Corrosion behavior of Cu−Al−Mn−Zn−Zr shape memory alloy in NaCl solution

Mo-yang YIN[1], Zhou LI[1,2], Zhu XIAO[1,3], Yong PANG[1], Ya-ping LI[1], Zi-yan SHEN[1]

1. School of Materials Science and Engineering, Central South University, Changsha 410083, China;
2. State Key Laboratory of Powder Metallurgy, Central South University, Changsha 410083, China;
3. Key Laboratory of Non-ferrous Metal Materials Science and Engineering, Ministry of Education, Central South University, Changsha 410083, China

Abstract: The corrosion behavior of a copper-based shape memory alloy (Cu−Al−Mn−Zn−Zr) in 3.5 wt.% NaCl solution was investigated by means of potentiodynamic polarization measurements, electrochemical impedance spectroscopy (EIS) and X-ray photoelectron spectroscopy (XPS). At the beginning of corrosion, oxidation products formed on the surface of the shape memory alloy and constantly covered the reaction surface, resulting in the decrease of corrosion rate. After 4 d of immersion in NaCl solution, the corrosion product layer became thick and porous, leading to the increase of corrosion rate, and the corrosion reaction mechanism changed from polarization control to diffusion control. The diffusion impedance increased with increasing thickness of the oxide layer for the samples immersed in NaCl solution for 6−15 d. During the whole corrosion process, the reaction mechanism of the alloy changed and the corrosion resistance was improved continuously. The corrosion products mainly contained CuO, ZnO, Al_2O_3, MnO/Mn_2O_3, MnO_2 and $Al(OH)_3$. Transition of the corrosion products from Cu_2O to CuO and Al_2O_3 to $Al(OH)_3$ occurred during corrosion.
Key words: Cu-based shape memory alloy; corrosion behavior; polarization; diffusion impedance

1 Introduction

Copper-based shape memory alloy has some potential applications in the industry due to its low cost, wide hysteresis, superelasticity and good cold working properties [1−3]. When using shape memory alloy pipe joint for pipe connection, first expanding the shape memory pipe joint at low temperature (below its martensite transformation temperature) and connecting two pipes with it, then heating the connector at a relative elevated temperature, the shape memory alloy joint will restore its diameter to original value and hold the two pipes tightly [4]. A connector made by the shape memory alloy with wide hysteresis had a wide range of application temperatures [5]. Especially in marine engineering and petroleum engineering, the shape memory alloy pipe joint with wide hysteresis is an effective component on quickly plugging up the leakage in case of pipeline rupture caused by unexpected events [6].

Cu−Al−Mn shape memory alloy is a new kind of shape memory alloy due to good comprehensive mechanical properties and shape memory performance [7]. The researches on it mainly focused on composition design, plasticity, orderly and disordered transformation, thermoelasticity and stress-induced martensite phase transformation, heat treatment, intelligent application and other aspects [8]. In recent years, breakthroughs in plasticity and superelastic properties have made it

develop rapidly in applications [9]. KAINUMA et al [10] developed a ductile Cu−Al−Mn alloy with Al content lower than 18%, which showed excellent cold processing performance; however, the martensite in this alloy after the deformation was extremely easy to be stabilized, leading to the poor reversibility of the alloy. Previous study [9−11] showed that the designed Cu−Al−Mn−Zn−Zr alloy had wide hysteresis, superelasticity, good martensite stabilization resistance and excellent cold working properties, which could be an ideal candidate for low cost pipe joint. However, the corrosion properties could be evaluated when using in marine engineering industry.

In this work, the corrosion behavior of the wide hysteresis Cu−Al−Mn−Zn−Zr alloy under different annealing temperatures was characterized by potentiodynamic polarization measurements, electrochemical impedance spectroscopy (EIS) and X-ray photoelectron spectroscopy (XPS). The corrosion mechanism of the alloy in 3.5 wt.% NaCl solution was discussed.

2 Experimental

2.1 Alloy preparation

The alloy ingot was prepared by medium-frequency induction melting and iron mold casting (180 mm × 85 mm × 30 mm), with the raw materials of pure copper, aluminum, zinc and electrolytic manganese and Cu−Zr intermediate alloys. The composition of shape memory alloy is shown in Table 1. After removing the surface defects by mechanical milling, the ingot was homogenized at 850 °C for 2 h, and then hot-rolled 3 times to reduce the thickness from 20 to about 2.5 mm. The hot-rolled plate was then solution-treated at 800 °C for 20 min.

Table 1 Composition of test sample (wt.%)

Cu	Al	Mn	Zn	Zr
78.5	8.8	8.5	4	0.2

2.2 Electrochemical test

For corrosion tests, the samples with dimensions of 10 mm × 10 mm × 2 mm were cut from the solution-treated plate by wire cutting machine. The surfaces of all samples were ground using 1200 grit sand paper and polished. The samples were subsequently immersed in 90%

ethanol for 5 min to clean the surface, dried in hot air, and then immersed in 3.5 wt.% NaCl solution at room temperature ((25±2) °C).

The polarization and electrochemical impedance tests of samples immersed in 3.5 wt.% NaCl solution for different time were carried out on an IM6ex electrochemical workstation, using Pt as the auxiliary electrode and the saturated calomel electrode (SCE) as the reference electrode. An area of 1 cm^2 on the surface of sample was exposed in NaCl solution, while the other part was sealed with paraffin. All electrochemical measurements were performed after the open circuit potential (OCP) was stabilized. Samples immersed in NaCl solution for 0, 1, 3 and 6 d were tested by potentiodynamic polarization measurement. The scan range is from −0.6 to 0 V and step length is 1 mV/s. The experimental data was analyzed by Origin9. The samples immersed in NaCl solution for 0, 1, 3, 6, 10 and 15 d were tested by impedance spectra, with the AC voltage signal amplitude of 5 mV and the frequency between 10 mHz and 100 kHz. The impedance data were analyzed by Zview software.

2.3 X-ray photoelectron spectroscopy (XPS) analysis

The samples immersed in NaCl solution for 1 and 15 d were used to investigate the corrosion products of the designed alloy during corrosion. The corrosion product layer was measured by K$_\alpha$ 1063 X-ray photoelectron spectroscopy (thermal Fisher science), using a monochromatic Al K$_\alpha$ X-ray source. The spot diameter was 400 μm. The step length of wide scanning was 1 eV and step length of narrow scanning was 0.05 eV. High-resolution photoelectron spectra of Cu 2p, Al 2p, Zn 2p and Mn 2p were tested.

3 Results

3.1 Potentiodynamic polarization behavior

The polarization curve is widely used to monitor the corrosion rate of alloys. By analyzing the polarization curve, the corrosion current density (J_{corr}), corrosion potential (φ_{corr}) and polarization slopes (β_a and β_c) can be obtained. The corrosion rate and corrosion resistance of the sample can be analyzed by corrosion current density and corrosion potential. Figure 1 shows the polarization curves of

samples immersed in NaCl solution for different time. The curve recorded as 0 d indicates that a freshly polished specimen is exposed to newly-prepared NaCl solution.
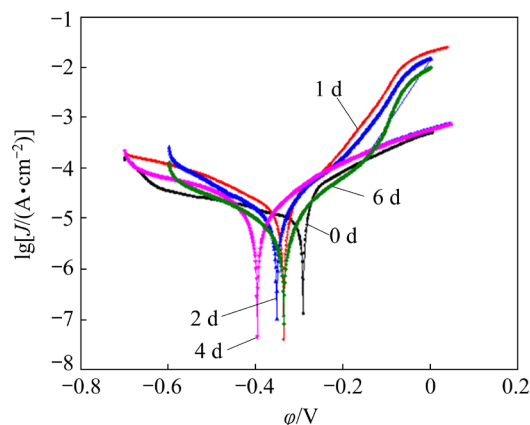

Fig. 1 Polarization curves of samples immersed in NaCl solution for different time

Since the analysis of the polarization curve must meet the polarization control conditions, the following equation can be used to fit the data within the range of ($\varphi_{corr} \pm 0.1$) V [12]:

$$J = J_{corr}\left[\exp\left(\frac{\varphi-\varphi_{corr}}{\beta_a}\right) - \exp\left(\frac{\varphi-\varphi_{corr}}{\beta_c}\right)\right] \quad (1)$$

where J and φ are the polarization current density and applied potential in the polarization curve, respectively, J_{corr} is the corrosion current density, φ_{corr} is the self-corrosion potential, and β_a and β_c are the anode and cathode Tafel slopes, respectively, which can be expressed as [13]:

$$\frac{1}{\beta_a} = \frac{d\ln|J_a|}{d\varphi}, \quad \frac{1}{\beta_c} = \frac{d\ln|J_c|}{d\varphi} \quad (2)$$

J_a and J_c are the anodic and cathodic current densities corrected for any changes in the reactant concentration on the electrode surface with respect to its bulk value, respectively.

Equation (1) shows the relationship between polarization current density and overpotential. The corrosion current density (J_{corr}) and Tafel slopes (β_a and β_c) can be fitted from the polarization curves. Table 2 shows the fitting results of electrochemical parameters. The Adj. R-square ($\overline{R}^2$) shows the goodness of fit, and can be computed by [14]

$$\overline{R}^2 = 1 - \frac{R_{SS}}{T_{SS}} \quad (3)$$

where T_{SS} is the total sum of square, and R_{SS} is the residual sum of square. The $\overline{R}^2$ values for the equivalent circuits are given in Table 2, which are close to 1.

Table 2 Corrosion current density J_{corr}, corrosion potential φ_{corr}, β_a, β_c and $\overline{R}^2$ of fitting results

t/ d	J_{corr}/ (μA·cm^{-2})	β_a/ V^{-1}	β_c/ V^{-1}	φ_{corr}/ V	$\overline{R}^2$
0	29.8	0.1483	−0.3515	−0.2920	0.9936
1	9.51	0.1162	−0.1902	−0.3370	0.9988
2	8.06	0.1173	−0.2017	−0.3516	0.9963
4	7.48	0.1211	−0.1896	−0.3770	0.9922
6	6.77	0.1499	−0.3217	−0.3366	0.9970

The corrosion current density decreases with the increase of the immersion time, indicating that the reaction rate of the alloy surface decreases continuously in the first 6 days. As the corrosion develops with time, the surface activity increases, leading to a decrease of the corrosion potential in the first 4 days. However, it increases at 6 d. The anodic Tafel slope decreases significantly at 1 d, then keeps stable, and rises again after corrosion for 4 d.

3.2 Impedance spectra

Figure 2 shows the electrochemical impedance spectra of samples immersed in NaCl solution for different time. The Nyquist spectra show a linear pattern in the high frequency zone and a semicircle pattern in the low frequency zone. The impedance spectrum at 0 d is composed of a high frequency capacitive reactance arc and a sloping line with a slope of 1, suggesting that the surface of the sample was smooth without oxidation product. Impedance spectra from 1 to 15 d contain the multiple time constant. With the increase of immersion time, the radius of the semicircle of Nyquist plot increases, suggesting that the charge transfer resistance of the oxide film increases with the immersion time. The width of the peak in the Bode plot in Fig. 2(b) increases with the increase of the immersion time, and two obvious peaks can be found in the Bode plots at the immersion time of 10 and 15 d. The phase angle of the sample exposed for 10 d is higher than that of sample exposed for 15 d in low frequency region.

According to the characteristics of the alloy and its impedance spectrum, three different

equivalent circuits were used to fit the impedance data of samples exposed in NaCl solution for different time. Three similar equivalent circuits were selected to describe the corrosion behavior of Cu−Al−Mn−Zn−Zr alloy in this study according to Ref. [15]. Table 3 shows the corresponding equivalent circuits used for fitting the impedance data. Equivalent elements are as follows: R_{sol} is resistance of the electrolyte; CPE_1 and CPE_2 are constant phase elements; R_{ct} is charge transfer resistance; R_{film} is resistance of the oxide film formed on the metal surface; W_o is semi-infinite Warburg impedance; W_s is finite Warburg impedance; χ^2 is the goodness of fit parameter.

Equivalent circuit I represents a sample with the bare surface of metal under semi-infinite diffusion condition. Equivalent circuits II and III refer to the two forms of $R_{sol}(CPE_1(R_{film}(CPE_2\ Z_f)))$ that is the equivalent circuit of electrode coated with an inert porous layer. Z_f is Faraday impedance on the electrode surface, which is the sum of charge transfer resistance and diffusion impedance. Without considering the diffusion impedance, Z_f can be replaced by charge transfer resistance, R_{ct}, in

Equivalent circuit II. If considering the contribution of diffusion to Faraday impedance, Z_f should be replaced by the diffused Warburg impedance (W_R) in series with a charge transfer resistance, and the equivalent circuit can be expressed with equivalent circuit III. For the corrosion process of copper alloys, equivalent circuit III was often used to characterize the diffusion impedance of ions inside the surface corrosion product layer [15].

The electric double layer formed on the surface can generally be equivalent to a capacitor. However, due to the influence of dispersion effect, the frequency response characteristics of the electric double layer are different from those of the pure capacitor. Therefore, the CPE is used to represent the electric double layer, and its impedance value (Z_{CPE}) can be given by the following equation [16]:

$$Z_{CPE}=Q(j\omega)^{-n} \tag{4}$$

where $1/Q$ is the admittance of the electrical double layer capacitance, j is the imaginary number ($j^2=-1$), ω is the angular frequency and n is the CPE exponent. The CPE exponent can be affected by the surface state of the electrical double layer. CPE is
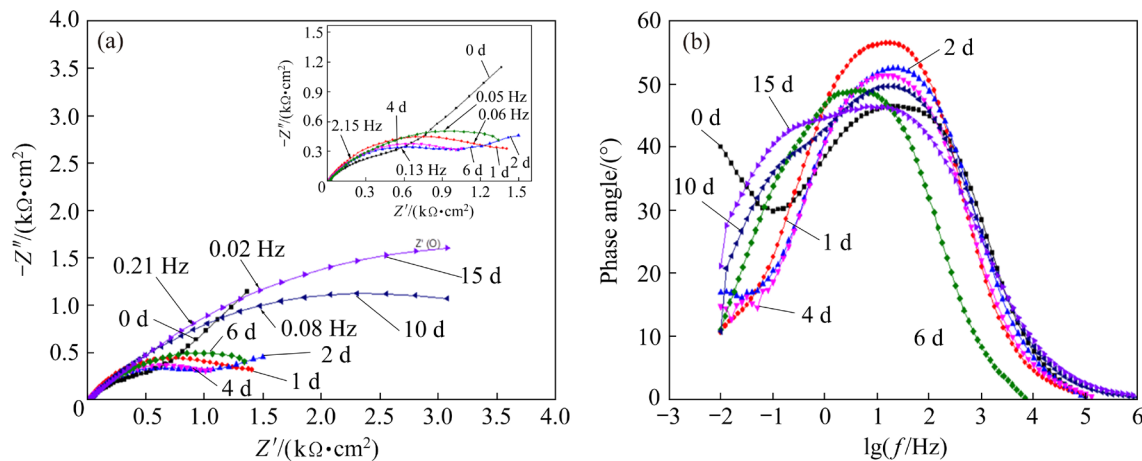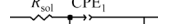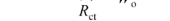

Fig. 2 Electrochemical impedance spectra of samples immersed in NaCl solution for different time: (a) Nyquist plots; (b) Bode plots

Table 3 Corresponding equivalent circuits and goodness of fit parameter (χ^2)

Equivalent circuit	No.	χ^2						
		0 d	1 d	2 d	4 d	6 d	10 d	15 d
	I	0.0002	−	−	−	−	−	−
	II	−	0.0004	0.0004	0.0009	0.0095	0.0011	0.0015
	III	−	0.0036	0.0012	0.0002	0.0003	0.0003	0.0003

equivalent to the pure resistance R for $n=0$, pure capacitance for $n=1$, and inductance L for $n=-1$, respectively.

The CPEs in Equivalent circuits I and II are equivalent to the capacitances of electric double layer or compact passive film. Q can be expressed as [17]

$$Q = \frac{d}{\varepsilon\varepsilon_0} \tag{5}$$

where ε is the dielectric constant, ε_0 is the permittivity of the free space and d is the thickness of the space charge layer [18].

The diffusion in the corrosion process can be expressed by Warburg impedance. When the thickness of diffusion stagnant layer is limited, Warburg impedance is denoted as W_s, and its impedance value (Z_W) can be given by the following equation [19]:

$$Z_W = \frac{W_R \tanh(j\omega T_1)^p}{(j\omega)^p} \tag{6}$$

where

$$T_1 = \frac{\delta^2}{D} \tag{7}$$

$$W_R = \sqrt{2}\sigma \tag{8}$$

where δ is the Nernst diffusion layer thickness, D is the average value of the diffusion coefficients of the species, and σ is the Warburg coefficient defined as

$$\sigma = \frac{RT}{\sqrt{2}n_1^2 F^2 A} \frac{1}{C_M \sqrt{D_M}} \tag{9}$$

where D_M is the diffusion coefficient of the metallic ion, A is the electrode surface area (1 cm²), n_1 is the number of transferred electrons, R is the molar

gas constant, F is the Faraday constant, T is the thermodynamic temperature, and C_M is the bulk concentration of the diffusing species. When the thickness of diffusion stagnant layer δ is much close to ∞, Warburg impedance can be expressed by semi-infinite diffusing impedance W_o. The imaginary part of the W_o impedance is equal to the real part. W_o is an oblique line with a slope of 1 in Nyquist plots.

In equivalent circuit III, the Warburg impedance is characterized the diffusion process inside the surface oxide product layer [20], δ, which represents the thickness of the film where the diffusion takes place.

According to the above analysis, impedance spectrum of 0 d sample was fitted by equivalent circuit I, and those of 1−15 d samples were fitted by equivalent circuits II and III, respectively. The Chi-square of the comparison results was calculated to select the best fitting model. The goodness of fit parameter χ^2 for each of the three equivalent circuits was calculated by the following equation [21]:

$$\chi^2 = \sum_{i=1}^{N} \frac{[Z_i' - Z'(\omega_i)]^2 + [Z_i'' - Z''(\omega_i)]^2}{\sigma^2} \tag{10}$$

where N is the number of data points, Z_i' and Z_i'' are the measured real and imaginary impedances, respectively, $Z_i'(\omega_i)$ and $Z''(\omega_i)$ are the calculated real and imaginary impedances from the model, respectively, and σ^2 is the variance of the measured data.

According to the data in Table 3, equivalent circuit II could be better to characterize the impedance spectrum of 1 and 2 d samples, while equivalent circuit III could characterize the impedance spectrum of 4, 6, 10 and 15 d samples. The fitting results are shown in Table 4.

Table 4 Elements of equivalent circuit for new alloy after being immersed in salt spray environment for different time

t/d	R_{sol}/ ($\Omega \cdot cm^2$)	Q_1/ ($\Omega^{-1} \cdot cm^{-2} \cdot s^n$)	n_1	R_{ct}/ ($\Omega \cdot cm^2$)	Q_2/ ($\Omega^{-1} \cdot cm^{-2} \cdot s^n$)	n_2	R_{film}/ ($\Omega \cdot cm^2$)	W_R/ ($\Omega \cdot cm^2$)	T_1	p	χ^2
0	7.144	7.21×10^{-4}	0.59763	598.4	−	−	−	5429	−	0.58207	0.0002
1	7.97	5.41×10^{-4}	0.68599	659.3	0.01553	0.79567	905.3	−	−	−	0.0004
2	7.002	3.68×10^{-4}	0.7593	803.6	0.001018	0.79567	804.15	−	−	−	0.0004
4	10.81	3.17×10^{-4}	0.71381	834.4	2.17×10^{-4}	0.67337	627.21	266.9	0.516	0.59195	0.0002
6	14.96	3.29×10^{-4}	0.81454	870.4	5.96×10^{-4}	0.60264	470.06	856.3	2.576	0.42939	0.0003
10	9.771	5.40×10^{-4}	0.65082	825.5	2.65×10^{-4}	0.5544	430.8	3258	4.898	0.57206	0.0003
15	10.67	5.54×10^{-4}	0.52746	796.5	1.54×10^{-4}	0.50005	370.5	6714	2.715	0.52616	0.0003

According to the results in Table 4, the corrosion products formed on the surface of the sample have a greater hindrance to corrosion reaction rate with the increase of corrosion time. In the impedance spectra of 0 to 6 d, the charge transfer resistance R_{ct} increases with the increase of the corrosion time. The growth rate of R_{ct} slows down at 4 and 6 d, and decreases slowly at immersion time of 10 and 15 d. There is a significant Warburg impedance in the 4−15 d impedance spectra, where W_R and T_1 increase with the increase of corrosion time. Although the R_{film} decreases with the increase of the corrosion time, the total impedance of the sample shows an upward trend.

During the corrosion process, oxidation products are constantly formed on the surface of the sample. It is speculated that during 1−2 d corrosion process, the alloy surface has not completely covered by corrosion products. But with the increase of the coverage area, the charge transfer resistance increases.

The results also show that Warburg impedance appears for impedance spectra at 4 and 6 d. W_R increases with the increase of corrosion time but is still less than R_{ct}, indicating that the corrosion product layer completely covers the surface of the alloy and influences the diffusion of ion [22]. The decrease of the surface area of the alloy makes the charge transfer resistance continue to increase, while the increase of ion concentrations in the porous oxidation product layer also makes R_{film} continuously decrease. However, with a small T_1 value and a thin oxide layer, the corrosion product layer has little influence on the diffusion, and the corrosion rate is still under the polarization-controlled.

In the impedance analysis results of 10−15 d, the charge transfer resistance decreases slowly, and W_R and T_1 values significantly increase, indicating that the corrosion product layer on the surface of the alloy becomes thicker and thicker according to Eqs. (6)−(8). The barrier for particle diffusion increases, and the control step of corrosion changes from polarization to diffusion. However, under the control of diffusion, the large decrease of R_{film} indicates that the concentration of ions in the surface oxidation layer increases and changes the concentration of reaction, resulting in the change of reaction rate and the slow decrease of R_{ct}.

3.3 XPS spectra

XPS measurement was performed on sample immersed in the 3.5 wt.% NaCl solution for 1 and 15 d. Figure 4 shows the wide XPS spectra of the corrosion product layer of the samples immersed in NaCl solution for 1 and 15 d. The main elements in the passive layer are Cu, Al, Mn, Zn, Cl and O. Zr was not detected due to its low concentration in the alloy.
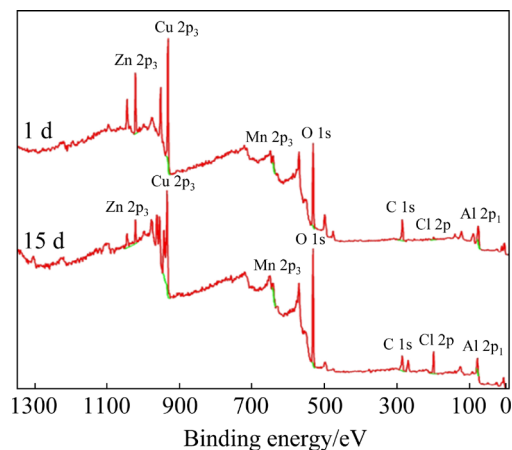

Fig. 3 Wide XPS spectra of corrosion product layer of samples immersed in NaCl solution for 1 and 15 d

3.3.1 Cu 2p spectra

Figure 4 shows the Cu 2p spectra of the corrosion product layer of sample immersed in NaCl solution for 1 and 15 d. The fitting parameters are given in Table 5. The spectrum of 1 d sample has a weak satellite peak at 943.6 eV and a main peak in Cu $2p_{1/2}$ spectrum with small full width. This is a typical characteristic spectrum of Cu_2O. The spectrum of 15 d sample has two strong Cu^{2+} satellite peaks at 943.6 and 963.0 eV, respectively. The peak in Cu $2p_{1/2}$ spectrum has wide full width. This is the typical characteristic spectrum of CuO. The peaks of metallic Cu and CuO are difficult to distinguish due to the small difference of binding energy between them. The Cu $2p_{3/2}$ spectrum is used to analyze the contents of Cu, Cu_2O and CuO quantitatively. The passive layer for 1 d sample contains 48.22% of Cu and 51.78% of Cu_2O, while that for 15 d sample contains 82.31% of CuO and 17.69% of Cu_2O.

The Cu 2p spectra confirmed from the electrochemical test that the passive film formed at earlier stage of corrosion was mostly Cu_2O. With the extension of the immersion time, the content of CuO increased significantly. The transition of the

corrosion layer surface principal component from Cu$_2$O to CuO occurred during the 30 d corrosion. The results are in accordance with Ref. [23]. CuCl and Cu$_2$(OH)$_3$Cl, which commonly appear in the corrosive layer [24], were not found in the present study.

3.3.2 Al 2p spectra

Figure 5 shows the Al 2p spectra of the corrosion product layer of sample immersed in NaCl solution for 1 and 15 d. The fitting parameters are given in Table 6. The peak intensity of the Al 2p slightly decreased during the corrosion process.

Al mainly exists in the form of Al$_2$O$_3$ and Al(OH)$_3$. Al$_2$O$_3$ is formed at the early stage of corrosion in the NaCl solution and its molar fraction decreases from 85.37% to 50.94% and the molar fraction of Al(OH)$_3$ increases from 14.63% to 49.06% when the immersion time increases from 1 to 15 d. The spectra also show the Cu 3p spectra caused by Cu and its corrosion products.

3.3.3 Zn 2p spectra

Figure 6 shows the Zn 2p spectra of the corrosion product layer of sample immersed in NaCl solution for 1 and 15 d. The fitting parameters

Table 5 Fitting parameters for Cu 2p spectra

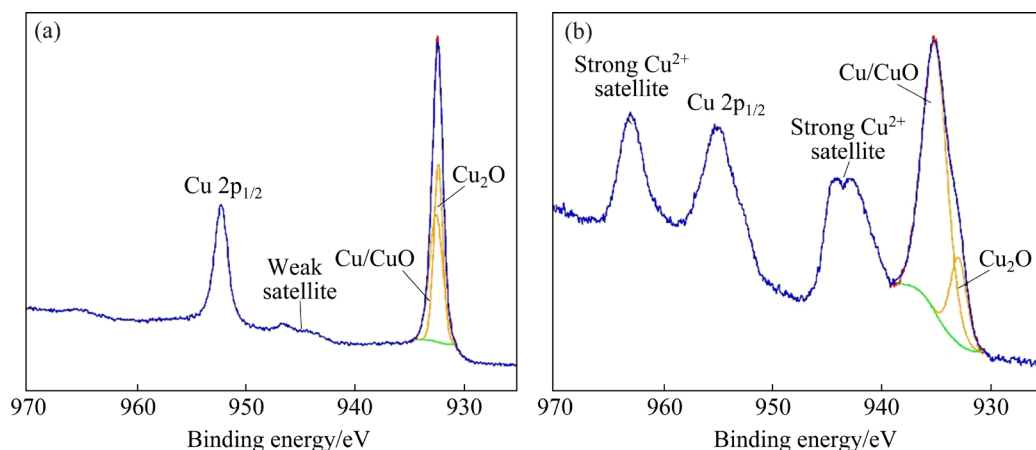| Immersion time/d	Proposed compound	Peak binding energy/eV	FWHM/eV	Molar fraction/%
1	Cu/CuO	932.37	0.96	48.22
	Cu$_2$O	932.58	1.46	51.78
15	Cu/CuO	935.1	2.67	82.31
	Cu$_2$O	932.91	1.79	17.69

Fig. 4 Cu 2p XPS spectra of corrosion product layer of sample immersed in NaCl solution for different time: (a) 1 d; (b) 15 d
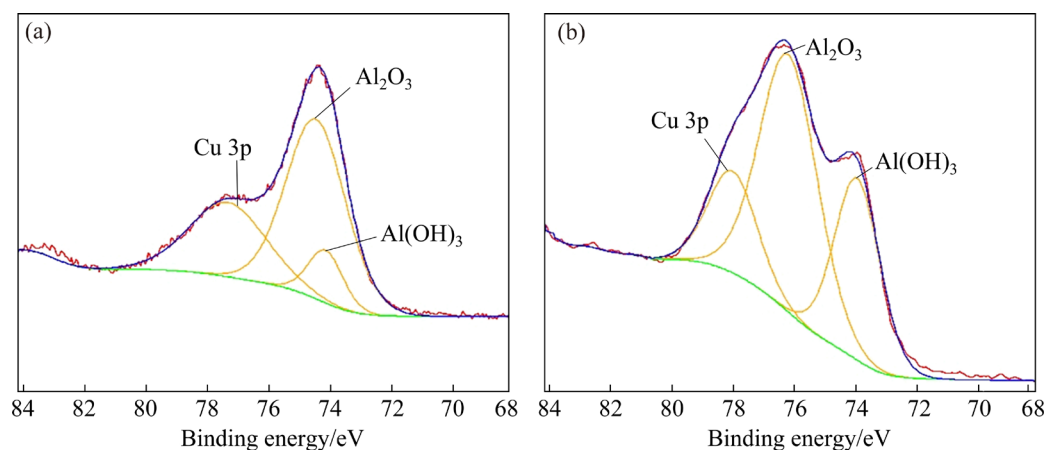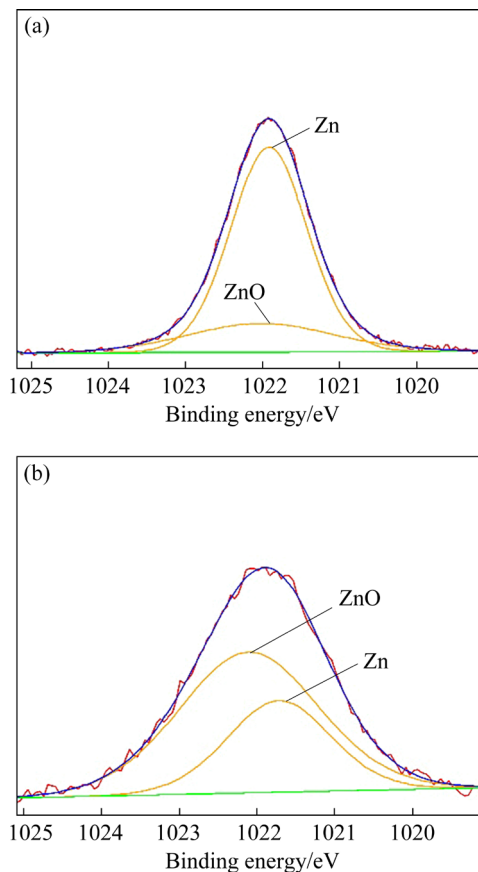

Fig. 5 Al 2p XPS spectra of corrosion product layer of samples immersed in NaCl solution for different time: (a) 1 d; (b) 15 d

Table 6 Fitting parameters for Al 2p spectra

Immersion time/d	Proposed compound	Peak binding energy/eV	FWHM/eV	Molar fraction/%
1	Al_2O_3	74.48	2.29	85.37
	$Al(OH)_3$	74.16	1.33	14.63
15	Al_2O_3	77.58	2.41	50.94
	$Al(OH)_3$	74.31	6.2	49.06

Fig. 6 Zn 2p XPS spectra of corrosion product layer of samples immersed in NaCl solution for different time: (a) 1 d; (b) 15 d

are given in Table 7. The peak at 1021.8 eV belongs to Zn and the other small peak at 1022.1 eV is attributed to ZnO. The peak intensity of Zn 2p decreases significantly and the molar fraction of ZnO in the corrosion product layer increases from 21.20% to 67.44% when the immersion time increases from 1 to 15 d. This suggests that dezincification occurs during the corrosion process.

3.3.4 Mn 2p spectra

Figure 7 shows the Mn spectra of the corrosion product layer of sample immersed in NaCl solution for 1 and 15 d. The fitting parameters are given in Table 8. The peak intensity of Mn 2p of sample immersed in NaCl solution for 15 d slightly decreases compared with that of sample immersed in NaCl solution for 1 d. Mn exists in the form of Mn, MnO, Mn_2O_3 and MnO_2. The molar fraction of Mn in the corrosion product layer decreases from 14.16% to 9.26%. The molar fraction of MnO/Mn_2O_3 and MnO_2 change little. These suggest that the contents of Mn and its oxides mainly decrease by the dissolution of the corrosion product layer.

4 Discussion

It has been generally accepted that the corrosion of the Cu-based alloys in neutral chloride solutions involves the cathodic reduction of oxygen [25,26]:

$$O_2+2H_2O+4e \rightarrow 4OH^- \tag{11}$$

The major anodic reactions of Cu dissolution are as follows [27]:

$$Cu+2Cl^- \rightarrow CuCl_2^- +e \tag{12}$$
$$2CuCl_2^- +H_2O \rightarrow Cu_2O+4Cl^-+2H^+ \tag{13}$$

Further oxidation of Cu, with the corrosion product of CuO, occurs with a prolonged immersion time under conditions of dissolved oxygen. Cu_2O could be oxidized to CuO through a sequence of reaction as follows [28]:

$$Cu_2O+O_2+H_2O \rightarrow 2CuO+H_2O_2 \tag{14}$$
$$Cu_2O+H_2O_2 \rightarrow 2CuO+H_2O \tag{15}$$
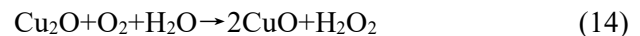
In the Zn-containing alloys, dezincification occurs because of the highly negative electrode potential in neutral chloride solutions:

$$Zn \rightarrow Zn^{2+}+2e \tag{16}$$

An additional passivation process occurs due to the formation of zinc oxide film during the dezincification process [29]:

$$Zn+H_2O \rightarrow ZnO+2H^++2e \tag{17}$$

An additional passivation reaction occurs in the chloride solution for alloy with Al addition. A layer of aluminum oxide is formed due to the surface dissolution of aluminum [30]:
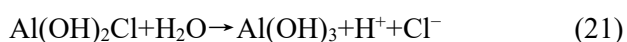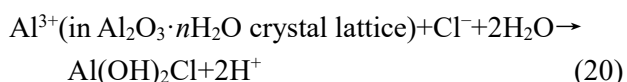
Table 7 Fitting parameters for Zn 2p spectra

Immersed time/d	Proposed compound	Peak binding energy/eV	FWHM/eV	Molar fraction/%
1	Zn	1021.87	1.75	78.8
	ZnO	1022.04	3.38	21.2
15	Zn	1021.72	1.56	32.56
	ZnO	1022.11	2.12	67.44

Table 8 Fitting parameters for Mn 2p spectra

Immersed time/d	Proposed compound	Peak binding energy/eV	FWHM/eV	Molar fraction/%
1	Mn	638.27	3.37	14.16
	MnO/Mn_2O_3	643.28	1.47	37.17
	MnO_2	641.47	2.94	48.67
15	Mn	638.74	3.24	9.26
	MnO/Mn_2O_3	641.49	3.25	46.30
	MnO_2	642.06	3.24	44.44
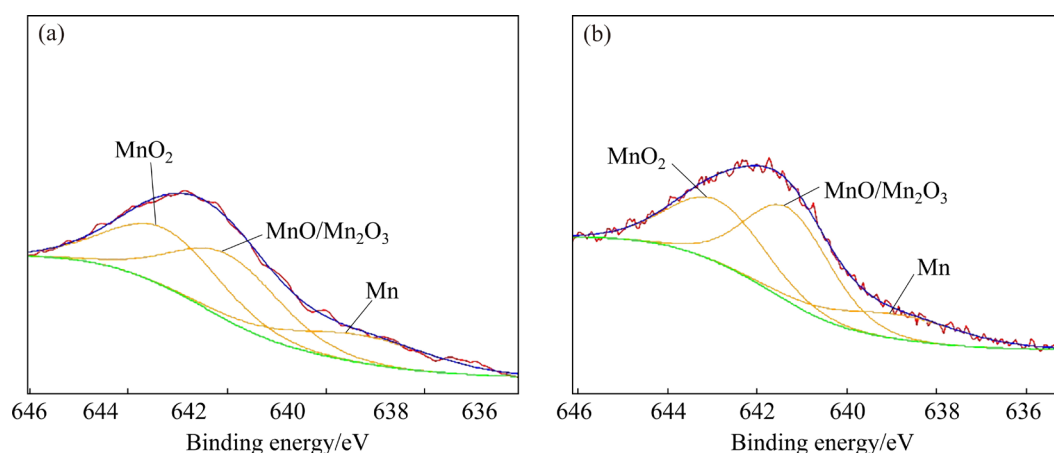
Fig. 7 Mn 2p XPS spectra of corrosion product layer of samples immersed in NaCl solution for different time: (a) 1 d; (b) 15 d

$$Al+4Cl^- \rightarrow AlCl_4^- +3e \tag{18}$$

$$AlCl_4^- +3H_2O \rightarrow Al_2O_3+6H^+ +8Cl^- \tag{19}$$

A dense Al_2O_3 film can protect the alloy from extensive corrosion but it may be continuously dissolved in chloride solutions according to Ref. [31]:

$$Al^{3+}(in\ Al_2O_3 \cdot nH_2O\ crystal\ lattice)+Cl^- +2H_2O \rightarrow$$
$$Al(OH)_2Cl+2H^+ \tag{20}$$

$$Al(OH)_2Cl+H_2O \rightarrow Al(OH)_3+H^+ +Cl^- \tag{21}$$

or

$$Al^{3+}(in\ Al_2O_3 \cdot nH_2O\ crystal\ lattice)+2Cl^- +2H_2O \rightarrow$$
$$Al(OH)_2Cl_2+2H^+ \tag{22}$$

$$Al(OH)_2Cl_2+H_2O \rightarrow Al(OH)_3+H^+ +2Cl^- \tag{23}$$
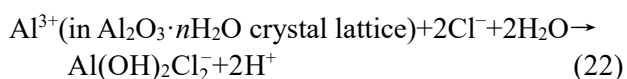
Progression of these reactions causes local acidity, thus accelerating dezincification and dealumination corrosion.

According to electrochemical analysis, for 0 d corrosion sample, Reactions (12) and (13) may take place. The oxidation products containing Cu_2O and Al_2O_3 are formed on the alloy surface during the first 4 d corrosion. The absolute value of Tafel slope after corrosion for 1 d is lower than that of 0 d, suggesting that the corrosion reactions in 1 d are much more active. This could be attributed to the generation of Cu_2O according to Reactions (14) and (15). According to potential−pH diagram of Cu−Cl−H_2O, Reactions (14) and (15) are more likely to occur than Reaction (13).

Although the Tafel slope of 1 to 4 d is almost

the same, the polarization current decreases and R_{ct} increases, suggesting that the reactivity of corrosion reaction increases but the total reaction rate gradually decreases, which could be attributed to the decrease of the corrosion reaction surface area. The porous oxide product is continuously formed on the surface of the alloy and completely covers the surface at 4 d corrosion according to the previous analysis of the impedance spectrum.

After 6 d corrosion, the diffusion impedance of porous oxide layer increases. In the porous oxide layer, the concentration of ions increases and pH declines, promoting the consumption of Al_2O_3 and the generation of $Al(OH)_3$. The reaction rates of Reactions (20)−(23) increase, leading to the decrease of the charge transfer resistance. The generation of $Al(OH)_3$ promotes the formation of porous oxide layer, thus significantly increasing the diffusion impedance and improving the corrosion resistance.

5 Conclusions

(1) With the extension of corrosion time, the corrosion current density measured by the polarization curve decreased, while the total impedance measured by the EIS increased continuously. The corrosion resistance of the Cu−Al−Mn−Zn−Zr shape memory alloy increased with increase of the immersion time in NaCl solution.

(2) EIS results showed that the corrosion reaction was mainly controlled by polarization for samples immersed in NaCl solution at the first four days, and further increasing the immersion time, the reaction was mainly controlled by diffusion.

(3) The corrosion product at the first day of corrosion mainly contained Cu_2O, ZnO, Al_2O_3, MnO/Mn_2O_3, MnO_2 and $Al(OH)_3$. After long time corrosion, a transition of the corrosion product from Cu_2O to CuO and Al_2O_3 to $Al(OH)_3$ occurred.

Acknowledgments

References

[1] OMORI T, KUSAMA T, KAWATA S, OHNUMA I, SUTOU Y, ARAKI Y, ISHIDA K, KAINUMA R. Abnormal grain growth induced by cyclic heat treatment [J]. Science, 2013, 341: 1500−1502.

[2] GOMIDŽELOVIĆ L, POŽEGA E, KOSTOV A, VUKOVIĆ N, KRSTIĆ V, ŽIVKOVIĆ, BALANOVIĆ L. Thermo-dynamics and characterization of shape memory Cu−Al−Zn alloys [J]. Transactions of Nonferrous Metals Society of China, 2015, 25(8): 2630−2636.

[3] VRSALOVIĆ L, IVANIĆ I, KOŽUH S, GUDIĆ S, KOSEC B, GOJIĆ M. Effect of heat treatment on corrosion properties of CuAlNi shape memory alloy [J]. Transactions of Nonferrous Metals Society of China, 2018, 28(6): 1149−1156.

[4] MOHD J J, LEARY M, SUBIC A, GIBSON M A. A review of shape memory alloy research, applications and opportunities [J]. Materials & Design, 2014, 56: 1078−1113.

[5] OCHONSKI W. Application of shape memory materials in fluid sealing technology [J]. Industrial Lubrication and Tribology, 2010, 62: 99−110.

[6] DUERIG T W, MELTON K N, STOCKEL D, WAYMAN C Y. Engineering aspects of shape memory alloys [M]. London: Butterworth-Heinemann, 2013.

[7] DRUKER A V, PEROTTI A, ESQUIVEL I, MALARRIA J. A manufacturing process for shaft and pipe couplings of Fe−Mn−Si−Ni−Cr shape memory alloys [J]. Materials & Design, 2014, 56: 878−888.

[8] LIU Ji-li, HUANG Hai-you, XIE Jian-xin. Superelastic anisotropy characteristics of columnar grained Cu−Al−Mn shape memory alloys and its potential applications [J]. Materials & Design, 2015, 85: 211−220.

[9] LI Zhou, WANG Ming-pu, Xu Ying-gen. Material of Cu-based shape memory alloys [M]. Changsha: Central South University Press, 2010. (in Chinese)

[10] KAINUMA R, TAKAHASHI S, ISHIDA K. Thermoelastic martensite and shape memory effect in ductile Cu−Al−Mn alloys [J]. Metallurgical and Materials Transactions A: Physical Metallurgy and Materials Science, 1996, 27(8): 2187−2196.

[11] SAUD S N, HAMZAH E, ABUBAKAR T, BAKHSHESHI-RAD H R, ZAMRI M, TANEMURA M. Effects of Mn additions on the structure, mechanical properties, and corrosion behavior of Cu−Al−Ni shape memory alloy [J]. Journal of Materials Engineering and Performance, 2014, 23(10): 3620−3629.

[12] ZHANG Jian-qing. Electrochemical measurement technology [M]. Beijing: Chemical Industry Press, 2010: 79. (in Chinese)

[13] GUIDELLI R, COMPTON R G, FELIU J M, GILEADI E. Defining the transfer coefficient in electrochemistry: An assessment (IUPAC Technical Report) [R]. Pure and Applied Chemistry, 2014.

[14] KASS R E, BATES D M, WATTS D G, SEBER G A F. Nonlinear regression analysis and its applications [J]. Technometrics, 1988, 32(2): 219−220.

[15] CAO Chu-nan, ZHANG Jan-qing. An introduction to electrochemical impedance spectroscopy [M]. Beijing: Science Press, 2002. (in Chinese)

[16] ORAZEM M E, TRIBOLLET B. The electrochemical society series: Electrochemical impedance spectroscopy [M]. Pennington: John Wiley & Sons, Inc., 2017, 9: 155−162.

[17] ŽAKLINA Z T, PETROVIĆ M M B, RADOVANOVIĆ M B. Cephradine as corrosion inhibitor for copper in 0.9% NaCl solution [J]. Journal of Molecular Structure, 2018, 1159: 46−54.

[18] BARSOUKOV E, MACDONALD R J. Impedance spectroscopy: Theory, experiment, and applications [M]. New Jersey: John Wiley & Sons, Inc., 2005.

[19] FRERS S E, STEFENEL M M, MAYER C, CHIERCHIE T. AC-Impedance measurements on aluminium in chloride containing solutions and below the pitting potential [J]. Journal of Applied Electrochemistry, 1990, 20(6): 996−999.

[20] MARTIN F J, CHEEK G T, O'GRADY W E, NATISHAN P M. Impedance studies of the passive film on aluminium [J]. Corrosion Science, 2005, 47(12): 3187−3201.

[21] DAISTRICK I D, MACDONALD J R, FRANCESCHETTI D R, MACDONALD J R. Impedance spectroscopy: Emphasizing solid materials and systems [M]. New York: John Wiley & Sons, Inc., 1987.

[22] DAWSON J L, JOHN D G. Diffusion impedance—An extended general analysis [J]. Journal of Electroanalytical Chemistry and Interfacial Electrochemistry, 1980, 110(1−3): 37−47.

[23] CHANG T R, HERTING G, JIN Y, LEYGRAF C, WALINDER I O. The golden alloy $Cu_5Zn_5Al_1Sn$: Patina evolution in chloride-containing atmospheres [J]. Corrosion Science, 2018, 133: 190−203.

[24] YUAN S J, PEHKONEN S O. Surface characterization and corrosion behavior of 70/30 Cu−Ni alloy in pristine and sulfide-containing simulated seawater [J]. Corrosion Science, 2007, 49(3): 1276−1304.

[25] METIKOŠ-HUKOVIĆ M, ŠKUGOR I, GRUBAČ Z, BABIĆ R. Complexities of corrosion behaviour of copper–nickel alloys under liquid impingement conditions in saline water [J]. Electrochimica Acta, 2010, 55(9): 3123−3129.

[26] PROCACCINI R, CERÉ S, VÁZQUEZ M. Oxygen reduction on Cu−Zn alloys [J]. Journal of Applied Electrochemistry, 2009, 39(2): 177−184.

[27] KEAR G, BARKER B D, STOKES K, WALSH F C. Flow influenced electrochemical corrosion of nickel aluminium bronze―Part I. Cathodic polarization [J]. Journal of Applied Electrochemistry, 2004, 34(12): 1235−1240.

[28] SANCHEZ S R D, BERLOUIS L E A, SCHIFFRIN D J. Difference reflectance spectroscopy of anodic films on copper and copper base alloys [J]. Journal of Electroanalytical Chemistry, 1991, 307(1−2): 73−86.

[29] CHEN Bang-yi, LIANG Cheng-hao, FU Dao-jun, REN De-ming. Corrosion behavior of Cu and the Cu−Zn−Al shape memory alloy in simulated uterine fluid [J]. Contraception, 2005, 72(3): 221−224.

[30] SÜRY P, OSWALD H R. On the corrosion behavior of individual phases present in aluminium bronzes [J]. Corrosion Science, 1972, 12(1): 77−80.

[31] WHARTON J A, BARIK R C, KEAR G, WOOD R J K, STOKES K R, WALSH F C. The corrosion of nickel−aluminium bronze in seawater [J]. Corrosion Science, 2005, 47(12): 3336−3367.

Cu−Al−Mn−Zn−Zr 形状记忆合金在 NaCl 溶液中的腐蚀行为

尹墨阳 [1]，李 周 [1,2]，肖 柱 [1,3]，庞 咏 [1]，李亚萍 [1]，沈紫嫣 [1]

1. 中南大学 材料科学与工程学院，长沙 410083；
2. 中南大学 粉末冶金国家重点实验室，长沙 410083；
3. 中南大学 有色金属材料科学与工程教育部重点实验室，长沙 410083

摘　要：通过动态电位极化测量、电化学阻抗谱 (EIS) 和 X 射线光电子能谱 (XPS) 研究铜基形状记忆合金 (Cu−Al−Mn−Zn−Zr)在 3.5% NaCl(质量分数)溶液中的腐蚀行为。腐蚀开始时，形状记忆合金表面形成的氧化产物不断覆盖合金表面，导致腐蚀速率降低。合金在 NaCl 溶液中浸泡 4 d 后，腐蚀产物层变厚及更加疏松多孔，导致腐蚀速率增大，合金表面的腐蚀反应机理由极化控制向扩散控制转变。在 NaCl 溶液中浸泡 6~15 d 后，试样的扩散阻抗随氧化层厚度的增加而增大。在整个腐蚀过程中，合金的腐蚀机理发生改变，耐蚀性能持续提高。腐蚀产物主要为 CuO、ZnO、Al_2O_3、MnO/Mn_2O_3、MnO_2 和 $Al(OH)_3$。腐蚀过程中腐蚀产物由 Cu_2O 转变为 CuO，由 Al_2O_3 转变为 $Al(OH)_3$。

关键词：铜基形状记忆合金；腐蚀行为；极化；扩散阻抗

(Edited by Wei-ping CHEN)